JMEPEG (2012) 21:1757–1762
DOI: 10.1007/s11665-011-0076-0
©ASM International
1059-9495/$19.00

Case Study: Pitting and Stress Corrosion Cracking in Heat-Affected Zone of Welded Underground 304 Stainless Steel Pipe

H.M. Tawancy and Luai.M. Al-Hadhrami

(Submitted August 24, 2010; in revised form October 3, 2011)

A jacketed underground pipeline made of 304 stainless steel tubing to transport utility water in a petrochemical plant at ambient temperature was perforated after few months of operation. Perforation started preferentially at the outer bottom surface of the pipe in the weld heat-affected zones where the insulating coating was damaged. Detailed microstructural characterization was carried out to determine the cause of failure using optical metallography, x-ray diffraction, scanning electron microscopy combined with energy dispersive spectroscopy, and transmission electron microscopy. Experimental results indicated that the failure occurred by interaction between the outer bottom surface of the pipe and surrounding environment leading to pitting and stress corrosion cracking in the presence of chloride ions. This could have been aided by residual welding stresses and the characteristic low stacking fault energy of the material.

Keywords electron microscopy, failure analysis, stainless steels

1. Introduction

Buried underground pipelines made of various grades of austenitic stainless steel tubing are commonly used in many applications in the petrochemical industry, e.g., hydraulic lines, utility water, and transporting hydrocarbons (Ref 1). This is because of their potentially useful combination of mechanical properties and corrosion resistance. It is well known that these steels derive their corrosion resistance from a thin tenacious surface layer of Cr_2O_3. Passivity is maintained in most natural environments; however, a transition to an active state occurs in environments containing high chloride concentrations as in seawaters or in reducing solutions. In this case, the protective oxide film is degraded by the chloride ions. Although pitting remains to be a problem in these environments (Ref 2-4), steel grades with lower pitting resistance can still be used provided that they are protected by insulating organic coatings (Ref 3, 5). However, pitting can still occur if the coating is damaged or cracked (Ref 6). The problem is compounded by the presence of residual tensile stress, e.g., in a weld heat-affected zone, causing stress corrosion cracking (Ref 7). Experiment shows that a correlation exists between stacking fault energy and the susceptibility to stress corrosion cracking, e.g., (Ref 1, 8). Alloys with lower stacking fault energy are more susceptible to cracking in comparison with those having higher stacking fault energy. Cracking can propagate both intergranularly and transgranularly and localized plastic deformation alongside grain boundaries has been shown to play an important role in intergranular stress corrosion cracking (Ref 9).

In extreme cases pitting can lead to perforation of tubing wall leaking highly flammable gases under pressure depending upon the particular application. Also, perforated water pipes can become unserviceable although less than 5% of the total metal is lost through rusting (Ref 7). In this study, an underground pipeline made of 304 stainless steel tubing and handling utility water in a petrochemical plant near seawater at ambient temperature was perforated after few months of operation. Corrosion was observed to exclusively occur at the external bottom surface of the pipe with some perforation limited to regions adjacent to weld seams. A section of perforated pipe was examined to determine the cause of failure.

H.M. Tawancy and **Luai.M. Al-Hadhrami**, Centre for Engineering Research and Centre of Research Excellence in Corrosion, Research Institute, King Fahd University of Petroleum & Minerals, P.O. Box 1639, Dhahran 31261, Saudi Arabia. Contact e-mail: tawancy@kfupm.edu.sa.

2. Experimental Procedure

Specimens from the pipe were examined both macroscopically and microscopically. Inductively Coupled Plasma-Atomic Energy Spectroscopy (ICP-AES) technique was used to measure the chemical composition of the pipe material. The carbon content was determined by analyzing the products of burning a specimen using gas chromatography. Metallographic specimens as well as samples of corrosion products were prepared from the pipe for detailed characterization by optical metallography, x-ray diffraction (Cu-K_α radiation) as well as various electron-optical techniques including scanning electron microscopy (SEM: JEOL 5800LV) combined with energy dispersive x-ray spectroscopy, and transmission electron microscopy (TEM: JEOL 2000EX). Specimens were examined both in the as-received, polished, and etched conditions. Etching was carried out in oxalic acid. Thin foils for transmission electron microscopy were prepared by the jet

polishing technique in a solution consisting of one part nitric acid and three parts methanol by volume. All foils were examined at an accelerating voltage of 200 kV. Microhardness measurement using Vickers hardness tester (200 g load) was used to evaluate the mechanical strength. At least five measurements were made in regions near the perforation and far from it.

3. Experimental Results and Discussion

Photographs illustrating a section of the pipe where perforation occurred are shown in Fig. 1. Corrosion product was observed at the outer bottom surface in the vicinity of the perforation; however, the internal surface was relatively clean. This is further illustrated in the optical macrographs of Figure 2 indicating that the pipe was corroded by interaction between the bottom surface and the surrounding environment particularly in those regions where the insulating coating was damaged.

Figure 3 summarizes typical microstructure and composition of a sound section of the pipe. As shown in the secondary electron image of Fig. 3(a), the microstructure revealed by etching was comparable to that of 304 stainless steel in the

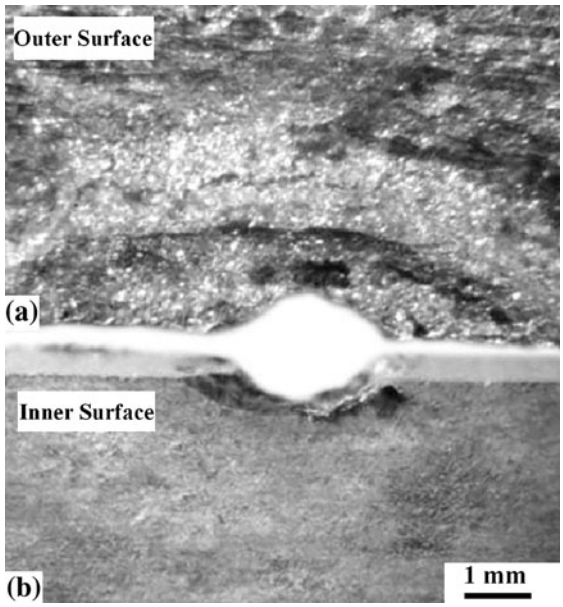

Fig. 2 Light optical macrographs of a section parallel to the surface showing macroscopic features of the outer and inner surfaces of the pipe in the vicinity of the perforation. (a) Outer surface, (b) inner surface

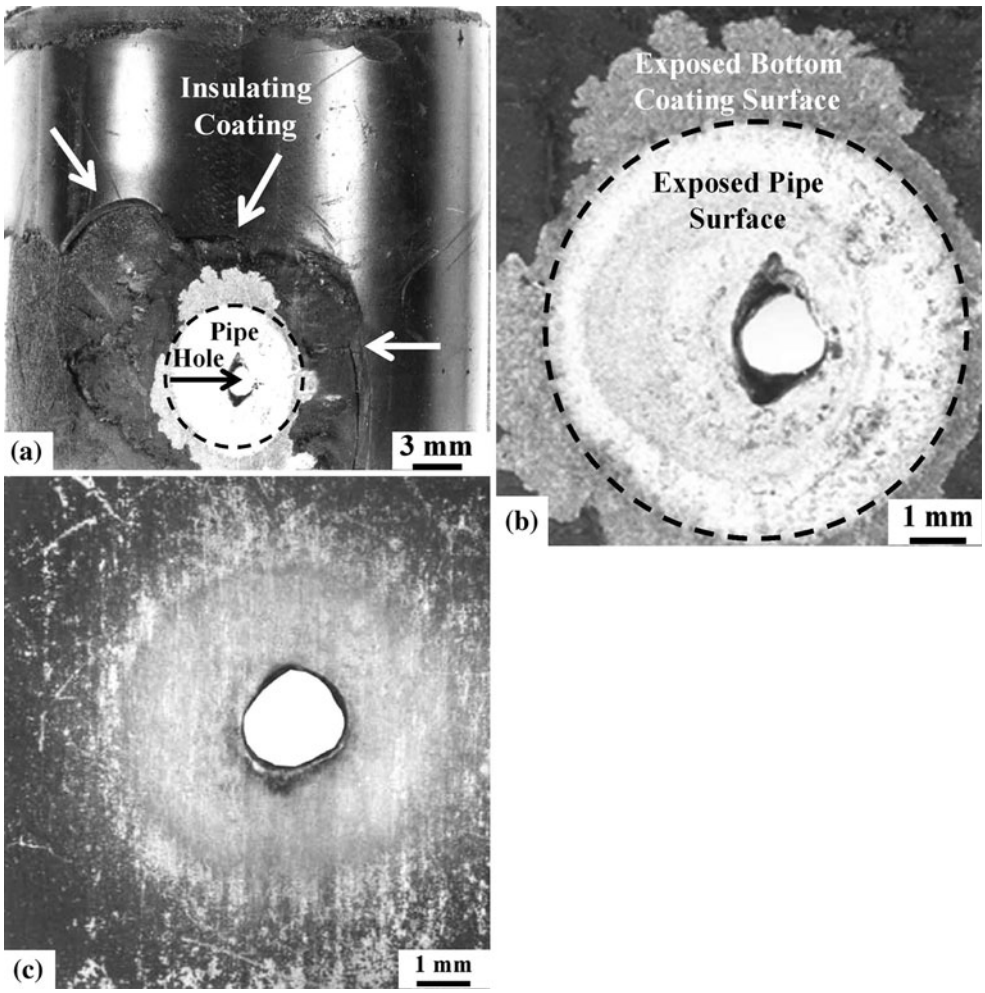

Fig. 1 Photographs illustrating general features of the pipe in the as-received condition. (a) An overall view of the outer surface of the bottom section of the pipe showing perforation in the region where the insulating coating was damaged. (b) A photograph showing the outer pipe surface. (c) A photograph showing the inner pipe surface

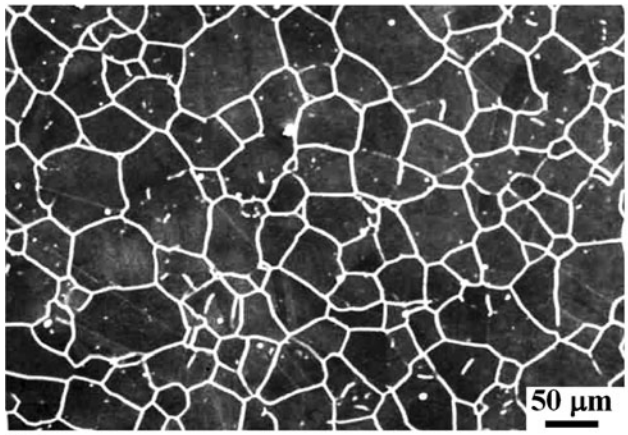

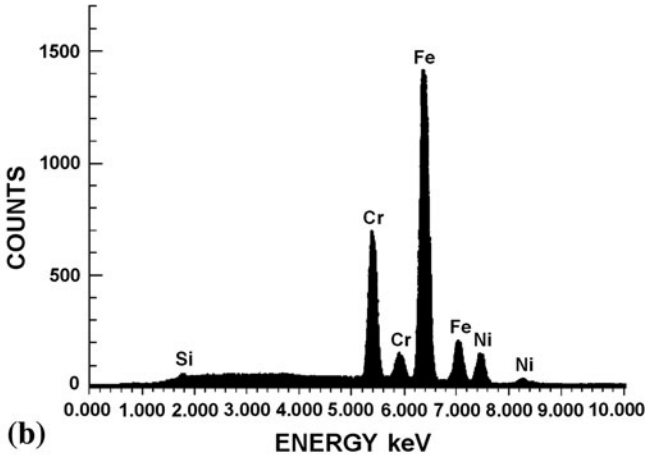

Element	Fe	Cr	Ni	Mn	Si	C	P	S
Nominal	Balance	18-20	8-12	2*	1*	0.08*	0.045*	0.03*
ICP-AES	Balance	18.72	9.95	0.93	0.57	0.026	0.032	0.020

(c) *maximum

Fig. 3 Typical microstructure and composition of a sound section of the pipe. (a) Secondary electron image showing the grain structure in the etched condition; scattered carbide particles are distinguished throughout the microstructure. (b) Corresponding energy dispersive x-ray spectrum illustrating the elemental constituents of the pipe material. (c) Nominal chemical composition of 304 stainless steel in comparison with that measured by inductively coupled plasma atomic energy spectroscopy (ICP-AES)

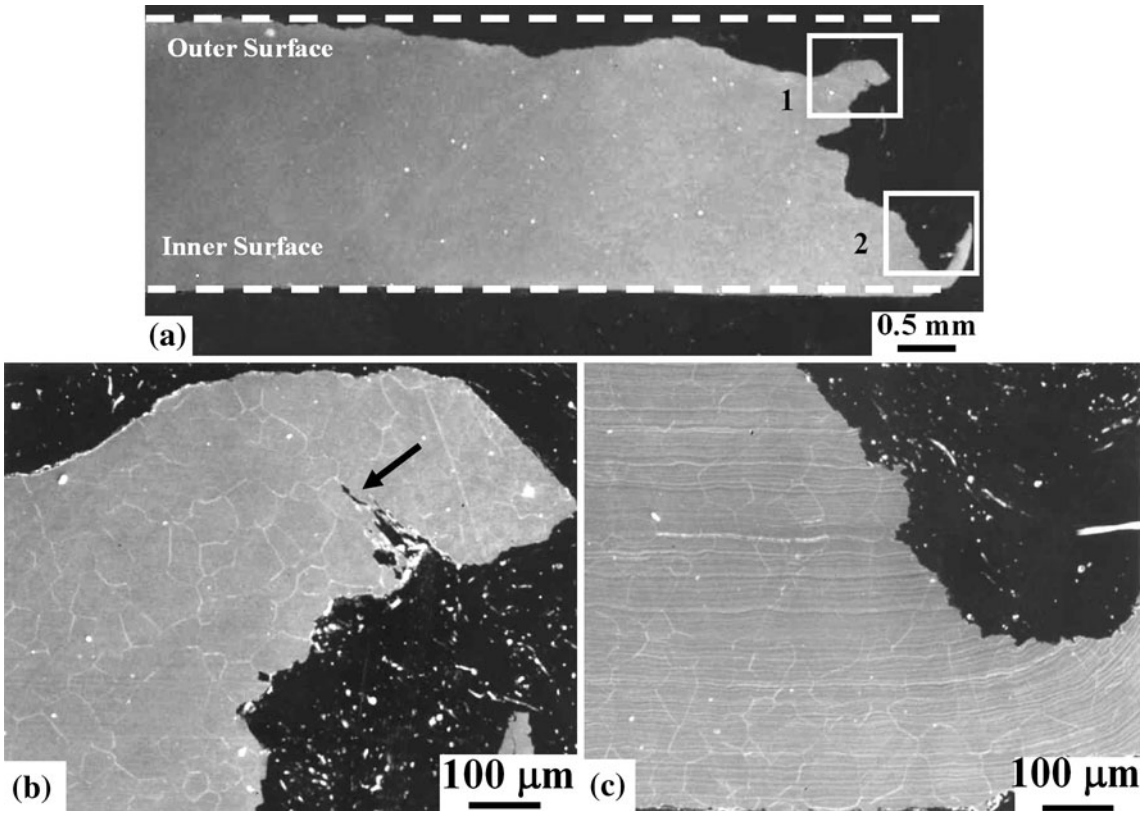

Fig. 4 Secondary electron images illustrating characteristic features of a cross section of the pipe near the perforation. (a) A macrograph indicating that tube wall thinning was initiated at the outer surface. (b) A micrograph showing the grain structure at the outer surface (region 1 in a); an intergranular crack is indicated by the arrow. (c) A micrograph showing the grain structure at the inner surface; absence of intergranular cracking is noted (region 2 in a)

annealed condition (Ref 10). A corresponding energy dispersive spectrum illustrating the elemental composition of the pipe is shown in Fig. 3(b) consistent with an alloy based upon the Fe-Cr-Ni system. Figure 3(c) summarizes the results of measuring the chemical composition by inductively coupled plasma atomic energy spectroscopy (ICP-AES) in comparison with the nominal composition of 304 stainless steel verifying that the pipe was manufactured according to specifications.

Consistent with the above results, examination of a cross section of the pipe indicated that the tube wall thinning eventually leading to perforation was initiated from the outer pipe surface as demonstrated in the secondary electron image of Fig. 4(a). Evidence for intergranular cracking at the outer surface was observed in the vicinity of the perforation as shown in Fig. 4(b). In contrast, there was no evidence for such cracking at the inner surface (Fig. 4c) suggesting that the cracking was also initiated at the outer surface of the pipe.

As shown in the example of Fig. 5, three types of grain structures could be distinguished throughout the pipe. A grain structure typical of annealed 304 stainless steel was observed in sound sections as demonstrated in Fig. 5(a) (specimen was polished and etched). Figure 5(b) shows a grain structure of a section subjected to corrosion attack near the perforation. Although the specimen was examined in the as-polished condition, the structure appears to be typical of a heavily etched material. Near the edges of the perforation at the outer surface, a structure such as that shown in Fig. 5(c) was observed in the as-received condition (unpolished and unetched), which typifies a fracture surface produced by intergranular separation. This observation is consistent with that of Fig. 4(b) showing intergranular cracking around the perforation at the outer pipe surface. Near the perforation, the average microhardness was measured to be HV 185, however, in far removed regions; the average microhardness was HV 162 comparable to that of annealed 304 stainless steel. Evidently,

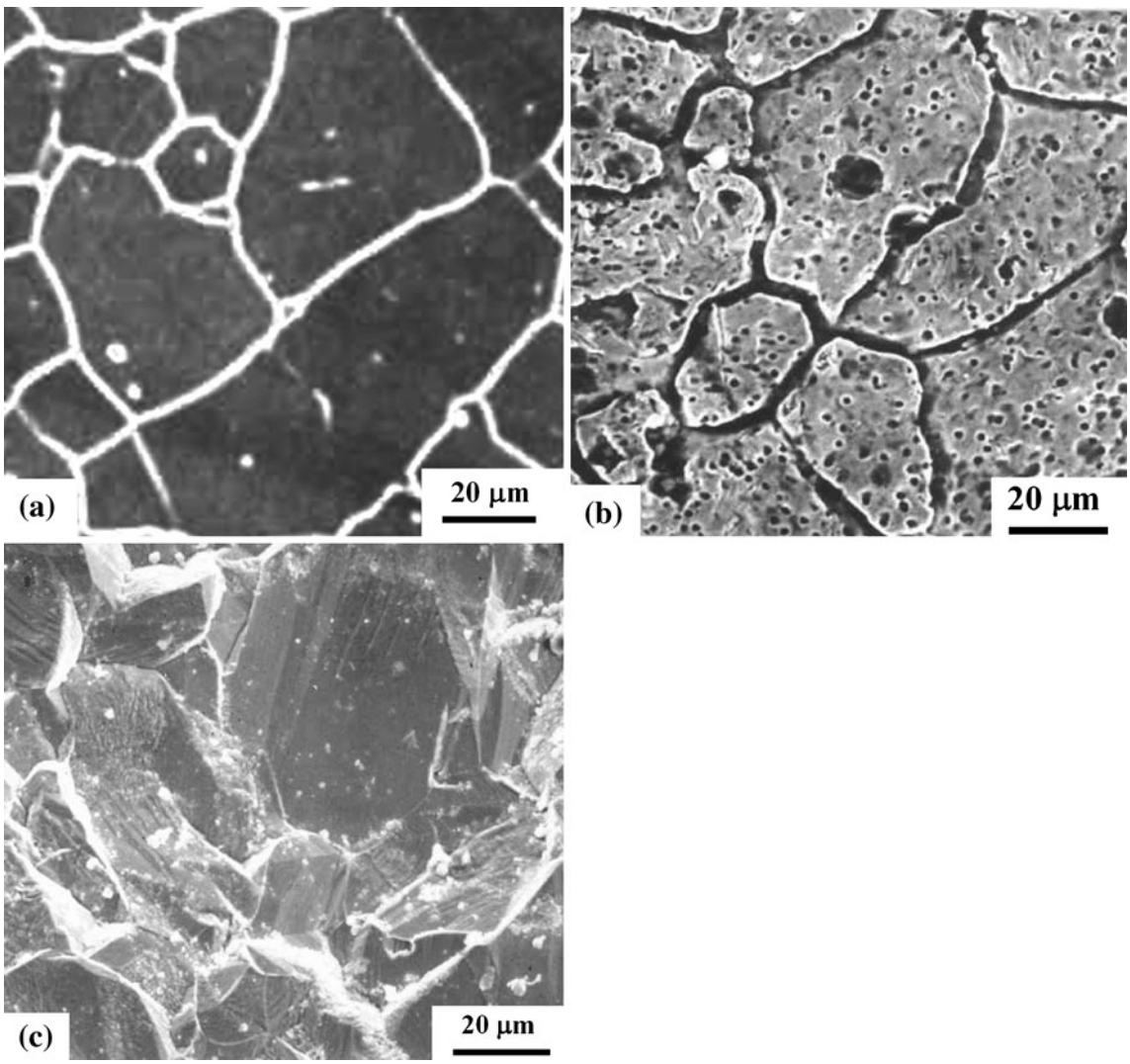

Fig. 5 Secondary electron images illustrating the three distinct grain structures observed in the perforated pipe. (a) Grain structure of a sound section of the pipe as revealed by etching. (b) Grain structure revealed by only polishing of the outer surface near the perforation. (c) Grain structure in the as-received condition (unpolished and unetched) derived from a region of the surface exposed by the perforation

the high hardness value near the perforation could be related at least partially to residual welding stresses.

Figure 6 summarizes the result of analyzing samples of corrosion product removed from the bottom surface of the pipe using x-ray diffraction. The observed diffraction pattern is compared with standard patterns of $FeCl_3$, $FeCl_2$, Fe_2O_3, and FeO(OH). An example illustrating the result of analyzing the corrosion product by energy dispersive x-ray spectroscopy in a scanning electron microscope is shown in Fig. 7. Combining the above results could lead to the conclusion that the corrosion product consisted of mixed iron chlorides and oxides indicating that the pipe was subjected to corrosion attack by chloride ions in defective regions of the insulating coating. However, the problem was further compounded by intergranular cracking suggesting that the pipe was subjected to both pitting corrosion and stress corrosion cracking. It is known that stress corrosion cracking of austenitic stainless steels is initiated at the grain boundaries (Ref 1). As pointed out earlier, this behavior could be related to localized deformation alongside grain boundaries. In this regard, examination of the deformation substructure in the vicinity of the perforation by transmission electron microscopy revealed features typical of a material with low stacking fault energy as described below.

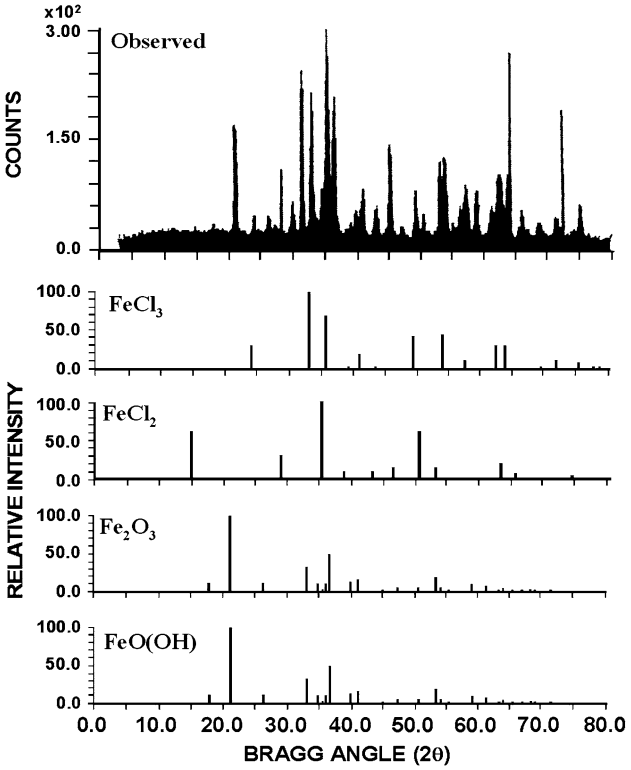

Fig. 6 An x-ray diffraction pattern derived from corrosion product collected from the outer surface of the pipe (observed) in comparison with standard ASTM patterns of $FeCl_3$, $FeCl_2$, Fe_2O_3, and FeO(OH)

Bright-field TEM images illustrating characteristic deformation substructures in various regions in the vicinity of the perforation are shown in Fig. 8a. A common feature was the observation of slip lines (traces of {111} slip planes) with dislocations mostly confined to their original slip planes as shown in Fig. 8a. This reflects a lower tendency for cross-slip associated with low stacking fault energy. At higher magnifications, extended nodes resulting from the intersection of three partial dislocations of the type $1/6\langle 112\rangle$ were observed as shown in the example of Fig. 8b. These observations are indicative of a material with high strain hardening rate, which is expected in many austenitic stainless steels. Detailed microstructural characterization down to the scale of transmission electron microscopy showed no evidence for sensitization particularly the presence of carbide precipitates at grain boundaries. Therefore, it is possible that as a result of high strain hardening rate, the grain boundaries became weaker than the matrix leading to localized intergranular separation in the presence of chloride ions.

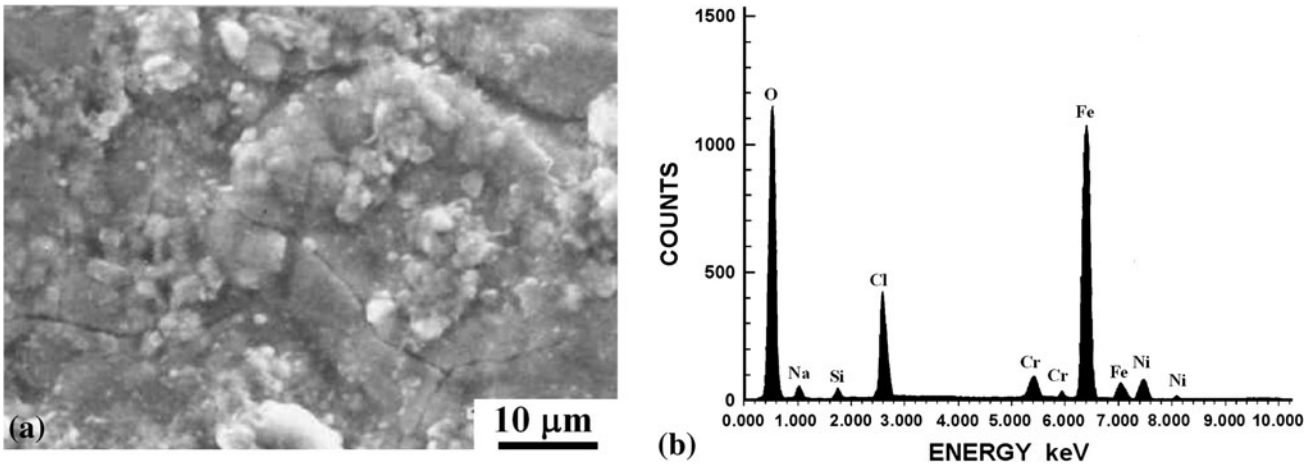

Fig. 7 An example illustrating the result of microchemical analysis of the corrosion product formed at the outer surface of the pipe by energy dispersive x-ray spectroscopy. (a) Secondary electron image showing the morphology of the corrosion product. (b) Corresponding energy dispersive spectrum illustrating the elemental composition of the corrosion product

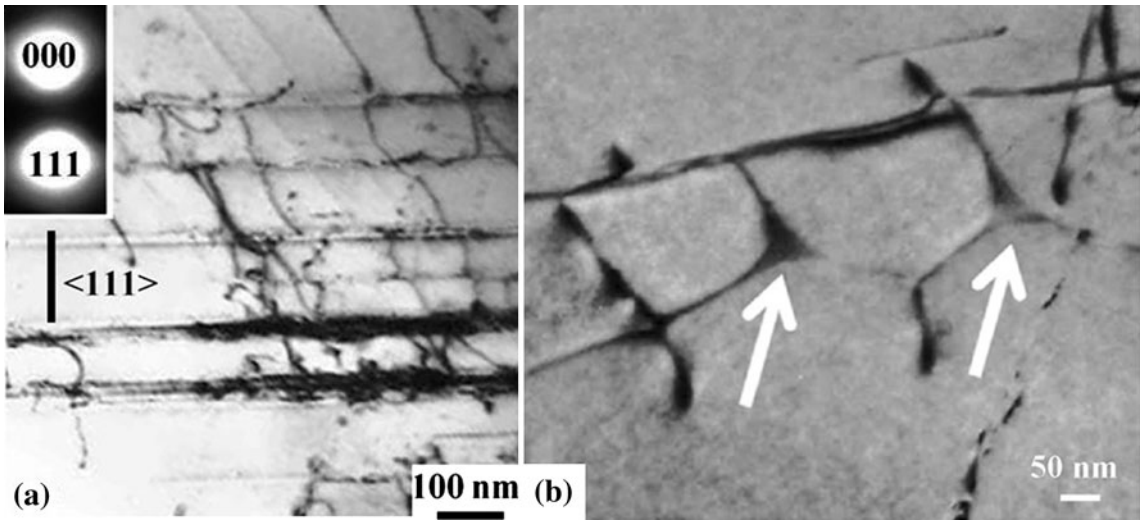

Fig. 8 Bright-field TEM images showing deformation substructures in the vicinity of the perforation typical of a material with low stacking fault energy. (a) Slip lines are visible with dislocations confined to their original slip planes. (b) Extended nodes resulting from interaction of three 1/6⟨112⟩ partial dislocations

4. Conclusion

It is concluded from the results of this study that perforation of the 304 stainless steel pipe in the weld heat-affected zone occurred by pitting corrosion and stress corrosion cracking in the presence of chloride ions. This could have been aided by a combination residual stresses and the characteristic low stacking fault energy of the material.

Acknowledgments

It is a pleasure to acknowledge the continued support of King Fahd University of Petroleum & Minerals and the Saudi Ministry of Higher Education.

References

1. K.H. Lo, C.H. Shek, and J.K. Lai, Recent Developments in Stainless Steel, *Mater. Sci. Eng. R*, 2009, **65**, p 39
2. Y. Gong, J. Cao, X.H. Meng, and Z.G. Yang, Pitting Corrosion on 316L Pipes, *Mater. Corros.*, 2009, **60**(11), p 899
3. G. Schiroky, D. Anibal, A. Okeremi, and C. Speed, Preventing Pitting and Crevice Corrosion of Offshore Stainless Steel Tubing, *World Oil*, April Issue (2009) p 73
4. M. Riahi and R. Alipour, Predictive Model for Determination of Pitting Corrosion in Stainless Steel Pipes, *Mater. Eval.*, 2004, **62**(3), p 373
5. E. Hur, G. Bereket, and Y. Sahin, Corrosion Inhibition of Stainless Steels by Polyaniline poly (2-Chloroaniline), and Poly (aniline-co-2-chloroaniline), *Prog. Org. Coat.*, 2006, **57**, p 149
6. F. Elshawesh, A. Elhoud, and O. Elraghai, Corrosion and Cracking Under Insulation of Type 304 Stainless Steel at Ambient Temperature, *Corros. Eng. Sci. Technol.*, 2003, **38**(3), p 239
7. P.A. Schweitzer, Stainless Steels, *Corrosion and Corrosion Protection Handbook*, P.A. Schweitzer, Ed., Marcel Dekker, New York, 1983, p 37–53
8. H.L. Logan, *The Stress Corrosion of Metals*, John Wiley and Sons, New York, 1966, p 129–136
9. K. Kishimoto, M. Kikuchi, T. Shoji, and M. Saks, Localized Deformation Induced Intergranular Stress Corrosion Cracking of Austenitic Alloys in Water, *Adv. Fract. Fail. Prev.*, 2004, **261**, p 885
10. ASM Metals Handbook, *Atlas of Microstructures of Industrial Alloys*, Vol 7, 8th ed., ASM International, USA, 1973, p 134